Hindawi Publishing Corporation
ISRN Mechanical Engineering
Volume 2013, Article ID 128326, 12 pages
http://dx.doi.org/10.1155/2013/128326

*Research Article*

# The Flow Simulation and Experimental Study of a Large Low-Head Mixed-Flow Pumping System

**Fan Yang and Chao Liu**

*College of Water Resource & Energy Power Engineering, Yangzhou University, Jiangsu, China*

Correspondence should be addressed to Fan Yang; sqyzyangfan@126.com

Received 1 July 2013; Accepted 6 August 2013

Academic Editors: O. P. Gandhi and A. Szekrenyes



A large low-head mixed-flow pumping system has been carried out based on numerical analysis of a three-dimensional viscous flow. For analysis, the Reynolds-averaged Navier-Stokes equations with a Shear stress transport turbulence model were discretized by finite-volume approximations. The result has shown that the flow in the double-helix volute passage is a spiral movement combining axial and rotary flows; the static pressure distribution in the volute is symmetric; the uniformity of axial velocity distribution and velocity-weighted average swirl angle at the outlet section is relatively low. The static pressure decreases gradually from the blade inlet to the exit on the pressure side, while increasing gradually on the suction side. The axial forces decrease gradually with the decrease of lifting head, and the radial forces decrease first and then increase. The pressure fluctuation at certain sections of the pumping system was measured from the model test. It is concluded that the pressure pulsations of impeller inlet and "$\omega$" back wall of inlet passage are little influenced by operating condition. The domain frequency of the impeller inlet is approximately equal to the rotation frequency, while that of double-helix volute passage is multiple relations with the rotation frequency.

## 1. Introduction

Mixed-flow pump, also known as diagonal flow pump, is a kind of pump types with higher specific speed. This kind of pump type has already got the extensive application in the farmland drainage, urban flood control, industrial drainage, or other fields. Mixed-flow pumping system is classified as volute style and guide vane style according to output structure species. Compared with the research on hydraulic performance of the axial-flow pump in [1–6], for the mixed-flow pump, few domestic and foreign scholars develop this study and obtain the relevant research results. Wu et al. in [7] studied on the interior flow characteristic and hydrodynamics performance of the open-type mixed-flow pump with various discharge structures. Lin et al. in [8] analyzed the flow in high specific speed mixed-flow pumps using an analytical method based on the two families of streamline surfaces theory (S1 and S2 streamline surfaces). A loss model for the mixed-flow pump impellers was developed by summarizing a variety of loss calculation formulas systematically in [9]. Felix et al. in [10] analyzed the states of steady flow and unsteady flow of mixed-flow pump and predicted the hydraulic performance quite accurately. Posa et al. in [11] used an immersed-boundary method to analyze the hydraulic performance of a mixed-flow pump. Kim et al. in [12] carried out high-efficiency design of a mixed-flow pump based on ANSYS CFX. The hydraulic characteristics of a volute-type discharge passage and the efficient pump device with new type volute passage of a large pumping station were performed based on numerical simulation and experiment in [13, 14].

In recent years, the researchers have been concentrated on the mixed-flow impeller design and flow field calculation; comparatively little investigation has been made on the large low-head mixed-flow pumping system. In this paper, in order to analyze the flow characteristics of the mixed-flow pumping system, a model with high efficiency was simulated by ANSYS CFX code under various conditions, and EN900 and water pressure sensor HM90 were used to measure pressure fluctuation of interior flow in this pumping system. Some meaningful conclusions were drawn, and it can provide some reference for pump station design and optimization.

## 2. Three-Dimensional Flow Model

*2.1. Governing Equations.* A commercial software package, ANSYS CFX from AEA Technology, was applied in the present paper. The three-dimensional Reynolds-averaged Navier-Stokes equations are solved. Assuming that the fluid is incompressible, the mass conservation and momentum equations can be expressed as follows:

$$\frac{\partial \overline{u}_j}{\partial x_j} = 0, \tag{1}$$

$$\frac{\partial}{\partial t}\left(\rho \overline{u}_i\right) + \frac{\partial}{\partial x_j}\left(\rho \overline{u_j u_i}\right) = \frac{\partial p^*}{\partial x_i} + \frac{\partial}{\partial x_j}\left[\mu_{\text{eff}}\left(\frac{\partial \overline{u}_i}{\partial x_j} + \frac{\partial \overline{u}_j}{\partial x_i}\right)\right] + f_i, \tag{2}$$

where $p^*$ denotes the converted pressure, $u_j$ is the velocity component, $\rho$ is the fluid density, $\mu_{\text{eff}}$ is the effective viscous coefficient, and $\mu_{\text{eff}} = \mu + \mu_t$, $\mu$ is the fluid dynamic viscosity.

The Reynolds-averaged Navier-Stokes equations were dispersed using finite-volume approximations, and the shear stress transport (SST) turbulence model was used as a turbulence closure. In the SST model, a $k$-$\omega$ model was used in the near-wall region, and a $k$-$\varepsilon$ model was used beyond the wall region. And a blending function ensured a smooth transition between the two models. The SST two-equation turbulent model is expressed for Eddy viscosity coefficient $\nu_t$, turbulent kinetic energy $k$ and turbulence frequency $\omega$, respectively, is as follows:

$$\nu_t = \frac{a_1 k}{\max\left(a_1\omega; \Omega F_2\right)}, \quad \nu_t = \frac{\mu_t}{\rho},$$

$$\frac{\partial\left(\rho k\right)}{\partial t} = \nabla\cdot\left[\left(\mu + \frac{\mu_t}{\sigma_{k3}}\right)\nabla k\right] + p_k - \beta'\rho k\omega - \nabla\cdot\left(\rho U k\right),$$

$$\frac{\partial\left(\rho\omega\right)}{\partial t} = \nabla\cdot\left[\left(\mu + \frac{\mu_t}{\sigma_{\omega 3}}\right)\nabla\omega\right] + \left(1 - F_1\right)2\rho\frac{1}{\sigma_{\omega 2}\omega}\nabla k\nabla\omega + \alpha_3\frac{\omega}{\rho}p_k - \beta_3\rho\omega^2 - \nabla\cdot\left(\rho U\omega\right), \tag{3}$$

where $F_1 = \tanh(\arg_1^4)$ and $F_2 = \tanh(\arg_2^2)$,

$$\arg_1 = \min\left(\max\left(\frac{\sqrt{k}}{\beta'\omega y}, \frac{500\nu}{y^2\omega}\right), \frac{4\rho k}{CD_{k\omega}\sigma_{\omega 2}y^2}\right),$$

$$\arg_2 = \max\left(\frac{2\sqrt{k}}{\beta'\omega y}, \frac{500\nu}{y^2\omega}\right) \tag{4}$$

$$CD_{k\omega} = \max\left(2\rho\frac{1}{\sigma_{\omega 2}\omega}\nabla k\nabla\omega, 1.0\times 10^{-10}\right),$$

where $\beta' = 0.09$; $\alpha_1 = 0.5556$; $\beta_1 = 0.075$; $\sigma_{k1} = 0.85$; $\sigma_{\omega 1} = 0.5$; $\alpha_2 = 0.44$; $\beta_2 = 0.0828$; $\sigma_{k2} = 1$; $\sigma_{\omega 2} = 0.856$.

Figure 1: Perspective of the mixed-flow pumping system.

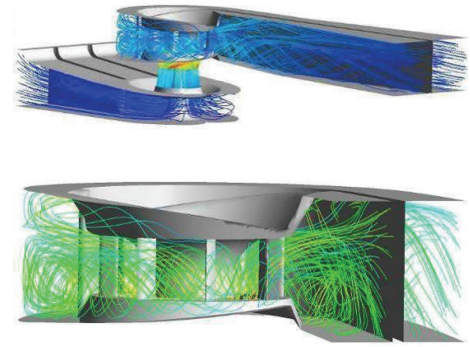

Figure 2: Internal particle path of mixed-flow pumping system.

*2.2. Geometry and Boundary Conditions.* Mixed-flow pumping system operating at 1450 r/min rotational speed is chosen as the sample for experimental. The diameter of the 4-bladed impeller is 300 mm. The tip clearance of impeller is 0.2 mm, which is the same as this of the experimental model. The computational domain includes bell-like inlet passage, impeller, double-helix volute passage with guide vane, and straight outlet passage (see Figure 1).

The structure grids for computational domains are generated using grid generation tool ANSYS Turbo-Grid for impeller, and the unstructured grids for computational domains are generated using grid generation tool ICEM CFD for inlet and outlet passages. The number of grid nodes is totally 1353170 for both rotating and stationary domains. The maximum of nondimensional wall distance $y^+ < 90$ has been obtained in the complete flow field.

Given the velocity of the bell-like inlet passage entrance, set the velocity distribution at the depth direction to logarithms distribution. Outflow boundary was set a certain distance far away from the outlet passage which was given in accordance with hydrostatic pressure distribution. The frozen rotor interfaces (FRI) were employed for calculations. The adiabatic and absolute no-slip boundary conditions are applied for the solid walls of the runner chamber, and the relative no-slip boundary conditions are applied for the solid walls of other flow passage components.

## 3. Computational Results

*3.1. Flow Field of the Pumping System.* The flow field of pumping system is shown in Figure 2. In the bell-like inlet passage, the flow is shaped like in a regular shrinkage way. The water flow against the pier goes along the guide cone into the impeller house, while the water flow against the outside wall

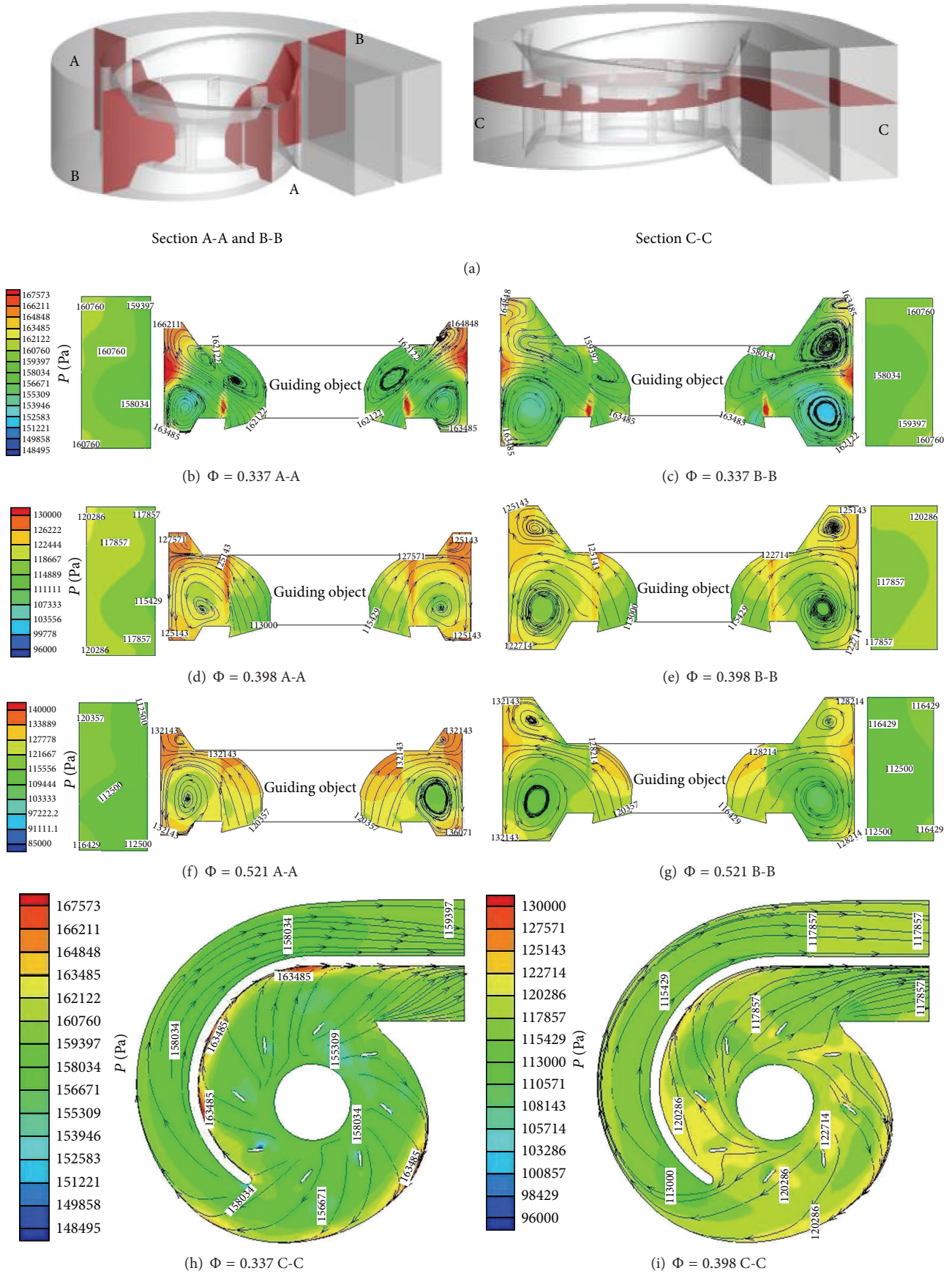


Figure 3: Continued.

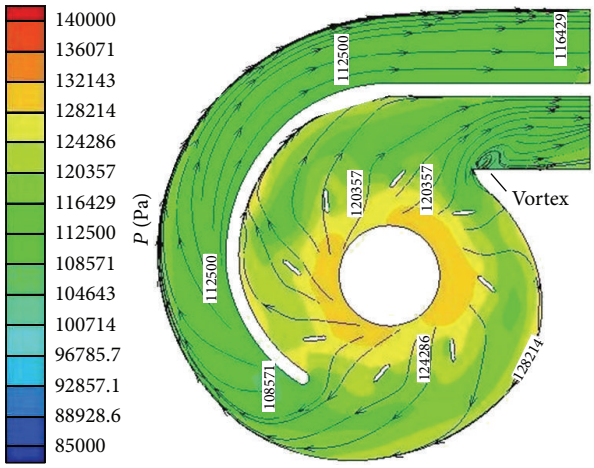


(j) Φ = 0.521 C-C

Figure 3: Static pressure contours and flow pattern of cross-sections in different conditions.

goes by passing the guide cone, through the "$\omega$"-shape back wall, and returns through the cone guide, into the impeller house from all around; in this part, it is shrinking gradually, smoothly, without reflow and whirling flow occurring.

Given that the impeller is rotating, volute type is recycling the pressure energy and controlling the circulation, when the water flow merges into the double-helix volute passage from all around; because of the constraints and the effects of the volute wall, the water flow against the pier, and the volute tongue is made comparatively complicated and the uneven flow speed. Especially, for the part inside the pier, the water flowing from top to bottom, and that from the sides to the outlet, merge into a whirling shape flow, feeding into the outlet passage, and at the two sides of the pier of the outlet, the water flow is whirling shaped. When looking into the water flow direction, the whirling is much stronger at the right side. Mainly it is caused by that the energy at the outlet of the impeller is not recycled well by the annular guide; therefore, the whirling water flow shaped by the complicated characteristic of the water flow and the undue structure of double-helix volute passage, causing the hydraulic loss, lowering the efficiency of the pump, and increasing the energy consumption.

*3.2. Hydraulic Performance of the Double-Helix Volute Passage.* Schematic diagram of key cross-sections in the double-helix volute passage is shown in Figure 3(a). Symmetrical static pressure distribution of cross-sections in the double-helix volute passage, inordinate flow pattern, and the existences of vortex is shown from the internal particle path in section A-A and section B-B under different working conditions. Through working done by mixed-flow impeller rotation, water oblique flow from the impeller house, the restriction effect of wall, and velocity difference between inner and outer surface cause vortex appearing; thus vortex may consume energy, at the same time increasing eddy current loss. At small large flow rate and optimum operating conditions, there is no vortex appearing in the volute tongue, and the flow pattern is steady. When looking into the water flow direction, flow turns to the left obviously at the right side of dividing pier, and flow turns to the right at the left side of dividing pier. The position of vortex appearing is shown in Figure 3(g) at large flow rate condition Φ = 0.521. There is great flow impact on the volute tongue at large flow rate condition, and velocity magnitude and direction change greatly, which easily bring vortex occurred.

In order to analyze quantitatively the hydraulic performance of double-helix volute passage, the uniformity of axial velocity distribution $V_{z+}$; the velocity-weighted average swirl angle $\theta$, the pressure recovery coefficient $\zeta$, and hydraulic loss $\Delta h$ have been calculated; among them, hydraulic loss mainly includes the route loss, eddy current loss, and mixture loss. Based on the hydraulic method, it is difficult to have relatively high computation precision for hydraulic loss, because the distribution of velocity field and pressure field is not steady, so that numerical simulation is a good method for calculation results of hydraulic loss. Calculation results are shown in Figure 4. In the range of Φ = 0.306~0.552, the indexes of hydraulic performance for volute-type outlet passage change along with flow rate; the curve of hydraulic loss is opening downward parabola; the curve of the pressure recovery coefficient is opening upward parabola, the minimal of which corresponds to that of hydraulic loss. The head loss of the passage is high to cause the efficiency of pumping system drop sharply under different working conditions. As the flow rate increases, the velocity-weighted average swirl angle increases gradually. The angle between lateral velocity and axial velocity decreases gradually, while flow rate increases, lateral velocity accounts for less percentage, and the velocity-weighted average swirl angle is lower than 75°, especially for low flow rate condition that is lower than 70°. The uniformity of axial velocity distribution decreases gradually, while flow rate increases, and as large flow increases in the same flow cross sections, velocity magnitude and direction change greatly, because the restriction effect of wall, so as to cause the uniformity of axial velocity distribution, is lower

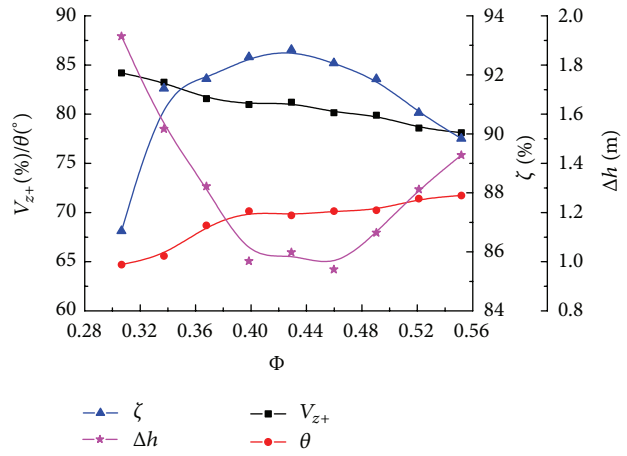


Figure 4: Performance curves of volute passage.

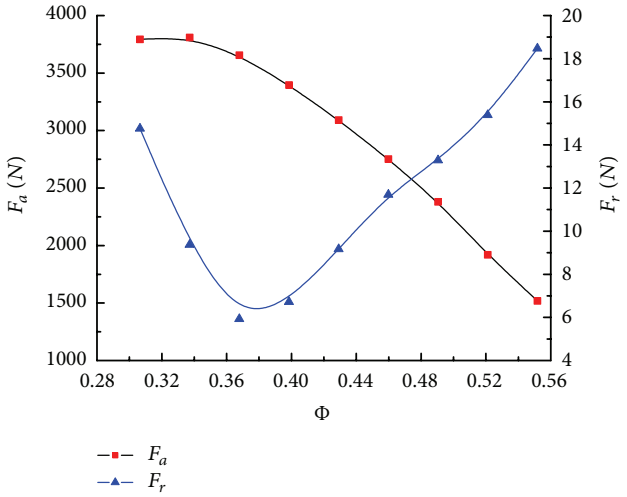


Figure 5: Axial forces and radial forces curves.

than 85%. The hydraulic performance of double-helix volute passage has important influence on the efficiency of pumping system.

*3.3. Hydraulic Performance of Impeller.* The rotation of impeller makes blade surface subject to axial force and radial force. Based on Computational Fluid Dynamics (CFD) numerical simulation, the force condition of impeller is analyzed under different working condition, and calculation result is shown in Figure 5. The axial force decreases gradually with the increase of flow rate, while the radial force decreases first and then increases. Radial force is very small in the high-efficiency area, which is beneficial to stable operation of pumping system.

Static pressure contours and wall streamlines of blades are shown in Figure 6, static pressure of the blade suction side (S.S.) increases gradually from the inlet edge to exit edge. Velocity difference between the front and back side makes static pressure in the head of blade drop sharply; blade pressure side (P.S.) has the high pressure region at the inlet edge, while blade suction side has the low pressure region at the inlet edge, because of flow around airfoil. With the increase of flow rate, negative pressure region at the inlet edge of blade suction side becomes increasingly great. Static pressure distribution of four blades is almost same under different working condition, which also shows that the uniformity of axial velocity distribution and velocity-weighted average swirl angle of outlet section is well, because the effect of the bell-like inlet passage rectifier. If the pressure distribution in four blades has a little difference, it will reduce deviation between working head and theoretical head. At $\Phi = 0.337$, the hub vortex is generated in the leading edge of the blade pressure side.

Distribution of static pressure in different spanwise position of the blade is shown in Figure 7. ($x/l$: control point is located in the chordwise position, where $x, l$ indicate the length of calculating point and wing tip, total chord length of hydrofoil). Static pressure is a relatively higher nearby blade flange, while static pressure is a lower nearby hub in the pressure side of the blade. Static pressure is a relatively lower nearby blade flange, while static pressure is the higher nearby hub in the blade suction side. Suction side of the blade inlet edge is the low-pressure region, easily to occur cavitation. More importantly, if pressure of root and middle in the blade suction side is lower than the vaporization pressure, it will cause a large area of suction side to occur cavitation and the efficiency of pumping system to drop, mainly because the pressure distribution is uniform in the middle of suction and pressure side.

*3.4. The Performance Prediction of Pumping System.* The simulated impeller is an adjustable mixed-flow pump with the specific speed $n_s$ of 670, and $n_s$ is defined between:

$$n_s = \frac{3.65N\sqrt{Q}}{H^{0.75}} = 3.65\left(\frac{\mathrm{r/\,min}\cdot\left(\mathrm{m^3/s}\right)^{1/2}}{\mathrm{m}^{3/4}}\right). \quad (5)$$

The rotor has 4 blades, and rotating speed $N$ is 1450 r/min, with the flow rate coefficient $\Phi = 0.460$, net lift $H$ of 7.05 m, and efficiency of 83.01% at blade angle $\beta = 0^\circ$.

For the performance presentations, the flow coefficient and the head coefficient were defined as follows:

$$\Phi = \frac{Q}{ND^3}, \qquad \psi = \frac{gH}{N^2D^2}, \quad (6)$$

where, $N$, $D$, $g$, and $H$ indicate the volume flow rate, rotating speed, diameter, acceleration of gravity, and the net lift of pumping system.

The hydraulic performance of pumping system, especially for hydraulic loss, depends mainly on the inner flow pattern of pumping system, which is closely related to geometry size of each part. The curves of hydraulic loss, experiment data of pumping system, and pump are shown in Figure 8; the characteristic performance curves by numerical simulation are the same tendency with that by test. Hydraulic loss of the inlet passage increases gradually with the increase of flow rate, while that of volute-type outlet passage decreases first and then increases, mainly because of outlet circulation of

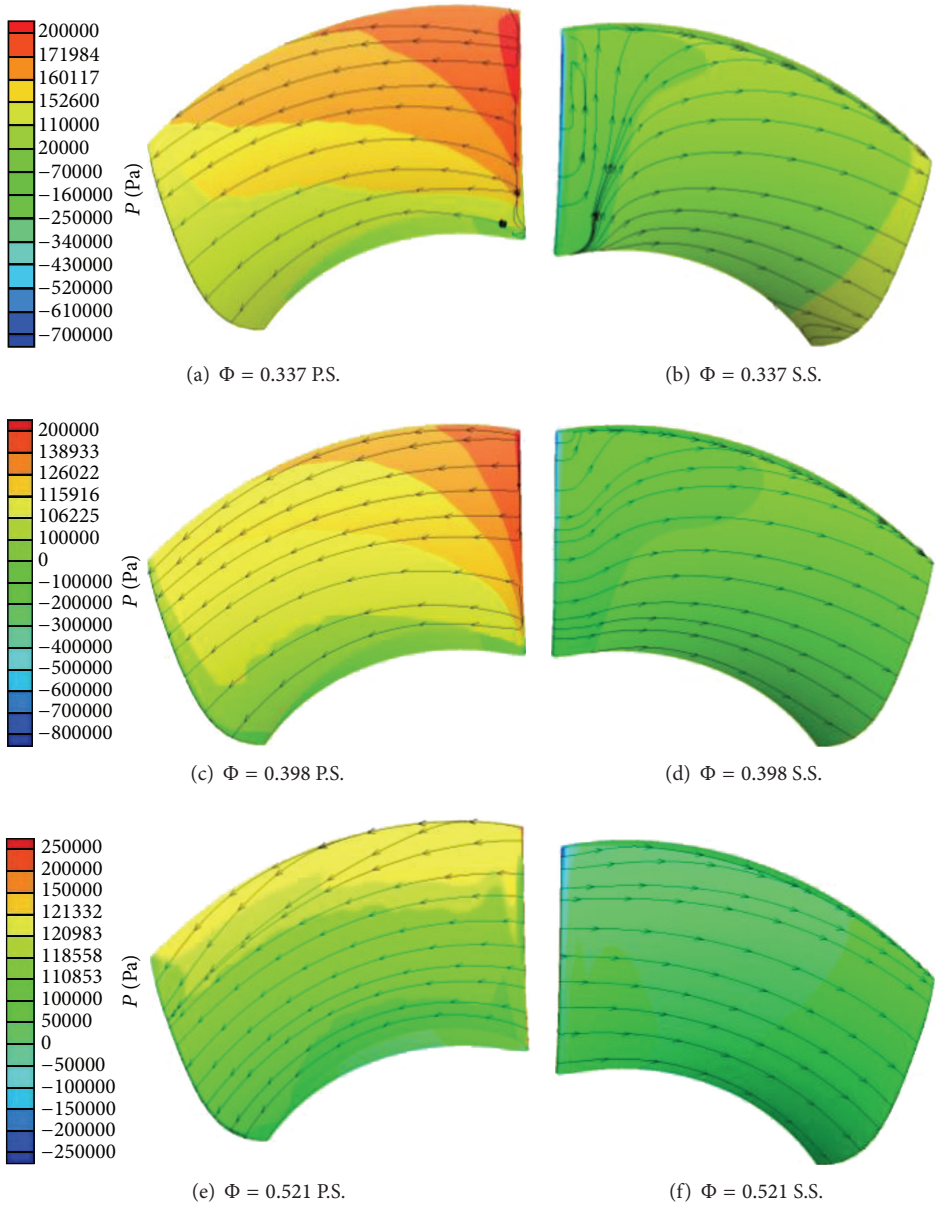


Figure 6: Static pressure contours and wall stream functions of blades.

impeller. The proportion of hydraulic loss of the double-helix volute passage in pumping system is between 68%~89%. Hydraulic loss of the straight outlet conduit increases, but with a little change with the increase of flow rate, because the recovery of circulation is different under different flow rate.

The curves of flow-lift curve and flow-efficiency curve are shown in Figure 9. Compared with numerical simulation results and experiment ones, a good agreement was found for lifting head between calculated and measured results. While the deviation of the efficiency between calculated and measured results does exist in nondesign points, the computational results are still unable to predict accurately the pumping system performance outside the high efficiency area, which need to be further improved.

## 4. Experimental Investigations

The purposes of model test are two: one is to verify the simulation results for credibility of the numerical simulation results, and other is to study the rules and characteristics of pressure fluctuation under different head with blade angle $\beta = 0^{\circ}$.

*4.1. Test System.* The test system is the high-precision hydraulic machinery test bed of Key Laboratory of Hydrodynamic Engineering of Jiangsu. The model pump is the National standard-size test pump, with the diameter of impeller as 300 mm.

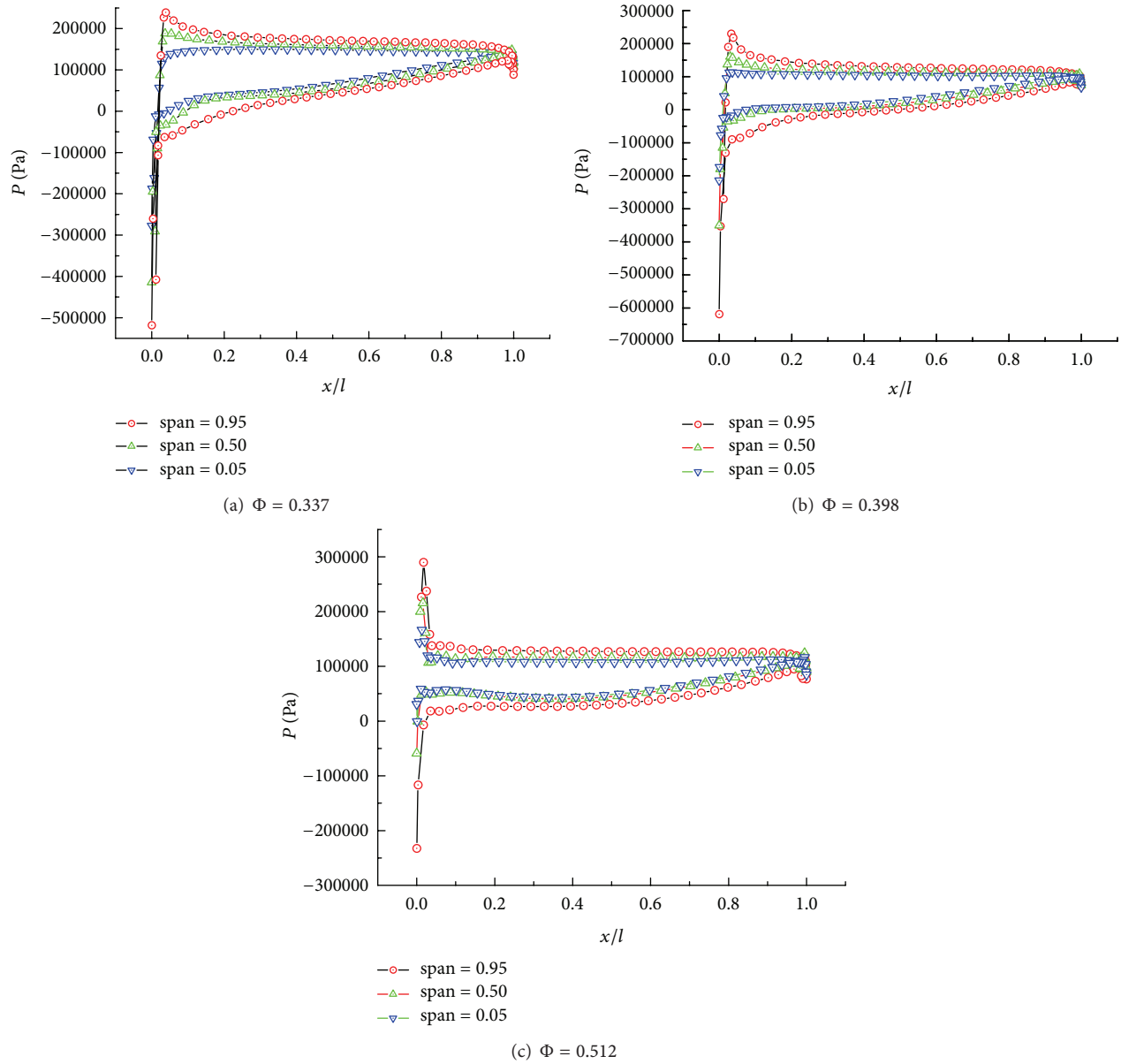


Figure 7: Static Pressure distribution on impeller blade of different discharges.

The comprehensive error of the test system is ±0.39% at design condition of the operation. Test equipment of the test system and the calibration accuracy of them are shown in Table 1.

The pumping system test bench is shown in Figure 10, and the picture of pumping system is shown in Figure 11.

*4.2. The Energy Performances of the Pumping System.* The synthetic characteristic curve was obtained by model test (see Figure 12). Compared with the vertical axial-flow pumping system, the efficiency of pumping system is lower, and the maximum efficiency of pumping system is 70.14% at blade angle $\beta = -4^\circ$ (see Table 2), because the hydraulic loss of the double-helix volute passage is higher.

*4.3. Pulsation Measurement of the Pumping System.* Pressure pulsation is the typical characteristics of hydrodynamics, which can indirectly reflect the dynamic information of inner flow characteristics. In order to study the rules and characteristics of pressure fluctuation for this kind of pumping system, three measuring points were arranged in "$\omega$" back wall of bell-like inlet passage, impeller inlet, and outer wall surface of double-helix volute passage, and the position of measuring point is shown in Figure 13. HM90 is the high frequency pressure pulsation sensor, and signal acquisition system is a portable digital testing equipment named ENVADA EN900. Test results is shown in Figure 14.

Pressure fluctuation of 3 measuring points were collected in 9 pumping system operating points at the blade angle 0°. The methods of amplitude and spectrum analysis were used

Table 1: Main parameters of test bed.

| Terms | Equipment | Type | Range | Calibration accuracy |
|---|---|---|---|---|
| Lifting head | Differential pressure transmitter | EJA110A | 0~200 kPa | ±0.113% |
| Flow rate | Electromagnetic flow meter | E-magDN400 | 100~500 L/s | ±0.197% |
| Torque and speed | Torque speed sensor | ZJ | 0~200 N·m<br>0~3000 r/min | ±0.108% |
| | Digital torque and speed routing indicator | TS-3100B | | ±0.0203% |
| *NPSH* | Pressure transmitter | EJA310 | 0~130 kPa | ±0.270% |

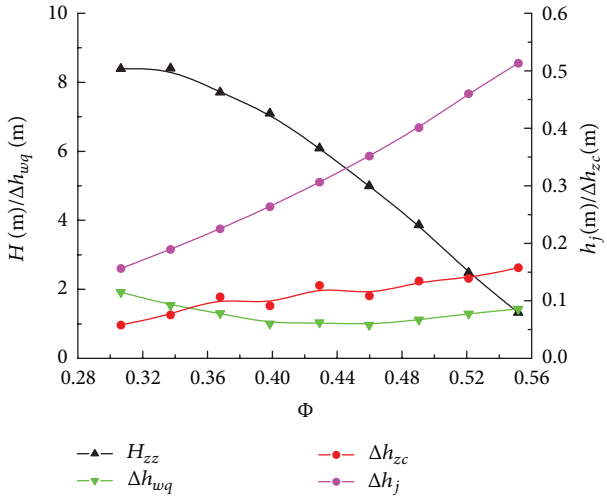


Figure 8: Curves of head and hydraulic loss.

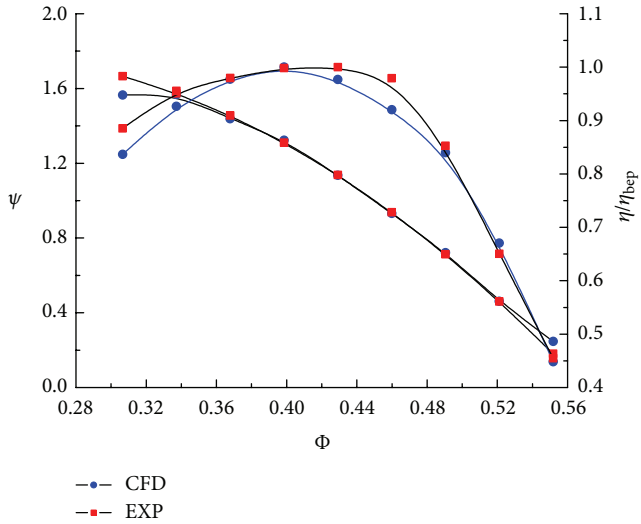


Figure 9: Performance curves of pumping system.

to analyze the test data. Amplitude analysis is the method of statistical characteristic values about samples. It is assumed that $x_1, x_2, \ldots, x_n$ are $n$ instantaneous value of samples. The meaning of each statistical parameter is as follows.

Figure 10: Test system of model pumping system.

Figure 11: Model pumping system.

Table 2: Performance parameters of model pumping system at BEP.

| $\beta$ | $\Phi$ | $\psi$ | $\eta$ (%) |
|---|---|---|---|
| −4° | 0.218 | 1.104 | 70.14 |
| −2° | 0.247 | 1.125 | 69.83 |
| 0° | 0.281 | 1.139 | 66.89 |
| +2° | 0.281 | 1.322 | 65.01 |
| +4° | 0.292 | 1.390 | 63.26 |

The mean $\overline{x}$ shows the time-averaged strength of pressure fluctuation:

$$\overline{x} = n^{-1} \sum_{i=1}^{n} x_i. \quad (7)$$

The interval-valued $z$ shows the amplitude of pressure fluctuation:

$$z = \max(x_1, x_2, \ldots, x_n) - \min(x_1, x_2, \ldots, x_n). \quad (8)$$

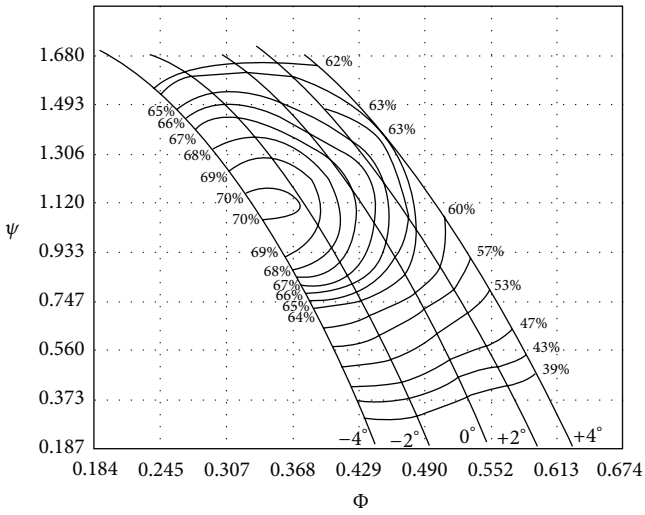


Figure 12: The synthetic characteristic curve of model pumping system.

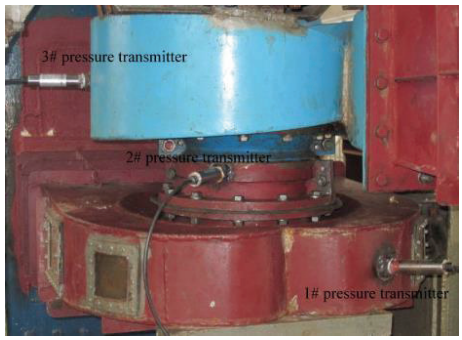


Figure 13: Installation drawing of pressure sensors.

The standard deviation $\sigma$ shows the difference of instantaneous value and mean, which is very important reference index of pressure fluctuation magnitude:

$$\sigma = \sqrt{n^{-1} \sum_{i=1}^{n} (x_i - \overline{x})^2}. \quad (9)$$

Besides, statistical parameter also includes maximum and minimum. Dimensionless quantity method was used to analyze and compare the test date. The ratio of statistical value to head was defined as $b$ in the same operating condition. The results of statistical analysis are shown in Figures 14(a), 14(b), and 14(c). The main frequency of each measuring point is shown in Figure 14(d).

Measuring point 1 stands for "$\omega$" back wall of bell-like inlet passage. Measuring point 2 stands for the inlet of the impeller. Measuring point 3 stands for the wall of double-helix volute passage. The relative quantity of the maximum value, minimum value, and average value of the pressure pulsation of measuring point 1 and measuring point 2 decreases with the increase of the head. When the traffic is high, the standard deviation of the pressure pulsation of measuring point 1 is 0.175, and the interval value is 0.0466. Compared to the standard deviation and interval value of measuring point 1 in other working conditions, both these two statistics are maximum. The discrepancy between the standard deviation and its minimum value is 0.0381, and the discrepancy between the interval value and its minimum value is 0.1598, which indicates that the range of variation of instantaneous pulsation is relatively large in this working condition. When the traffic is high in the working conditions, the velocity of the "$\omega$" back wall of inlet passage is quite higher, the flexing rate of flow line speeds up, and the intension of pulsation increases. It demonstrates that both the interval value and the standard deviation are higher. Nevertheless, the statistic itself is small. It indicates that the impacts of the rotation of the impeller on the "$\omega$" back wall of inlet passage are very small. The interval value and the standard deviation of the measuring point 2 also indicate that the statistic is maximum, and the range of pulsation is larger. The maximum value of the standard deviation is 0.0984. The statistical data of the pulsation of measuring point 3 do not present a whole regular pattern. However, when the traffic is high in the working conditions, each statistical datum is still very large, which indicates that the turbulent fluctuation in the volute is very large in the high-traffic working conditions. Figure 14(d) presents the dominant frequency of pulsation of each measuring point in different working conditions.

Figure 15 is the time-domain graph of each measuring point in the optimum operating condition ($\psi = 1.223$) and the high flow rate condition ($\psi = 0.383$). The rotation speed of impeller is 1450 r/min, and the rotation frequency of its impeller is 24.17 Hz. By analyzing the dominant frequency of pulsation of each measuring point in different operating conditions, it can be learned that the frequency of the flow tension and pulsation of the impeller inlet is the same with the rotation frequency of the impeller. The pulsation frequency of the inlet of impeller in different working conditions is affected by the rotation frequency of the impeller. The dominant frequency of the "$\omega$" back wall of inlet passage is two times of the rotation frequency of the impeller. The dominant frequency of the inlet of the impeller and the dominant frequency of the "$\omega$" back wall of bell-like inlet passage are not altered according to the variety of the working conditions. Within the range of testing head coefficient (0.224~1.493), the dominant frequency of pulsation and the rotation frequency of the impeller decrease with the increase of the traffic. The maximum dominant frequency of pulsation is four times of the rotation frequency of the impeller. The minimum dominant frequency of pulsation is one time of the rotation frequency of the impeller. The flow regime of the pressurized water chamber of the volute is influenced by the circular rector of the outlet of the guide vane to a large extent. From the time-domain graph of two operating conditions of measuring point 3 in Figures 15(e) and 15(f), it can be concluded that the range of pulsation of the double-helix volute passage does not present periodic fluctuation, especially when the traffic is large ($\psi = 0.383$), and the arbitrariness of the rang is large with the changing of time. It indicates that the flow regime in the pressurized water chamber of the volute is extremely turbulent. The main reason is that the remaining

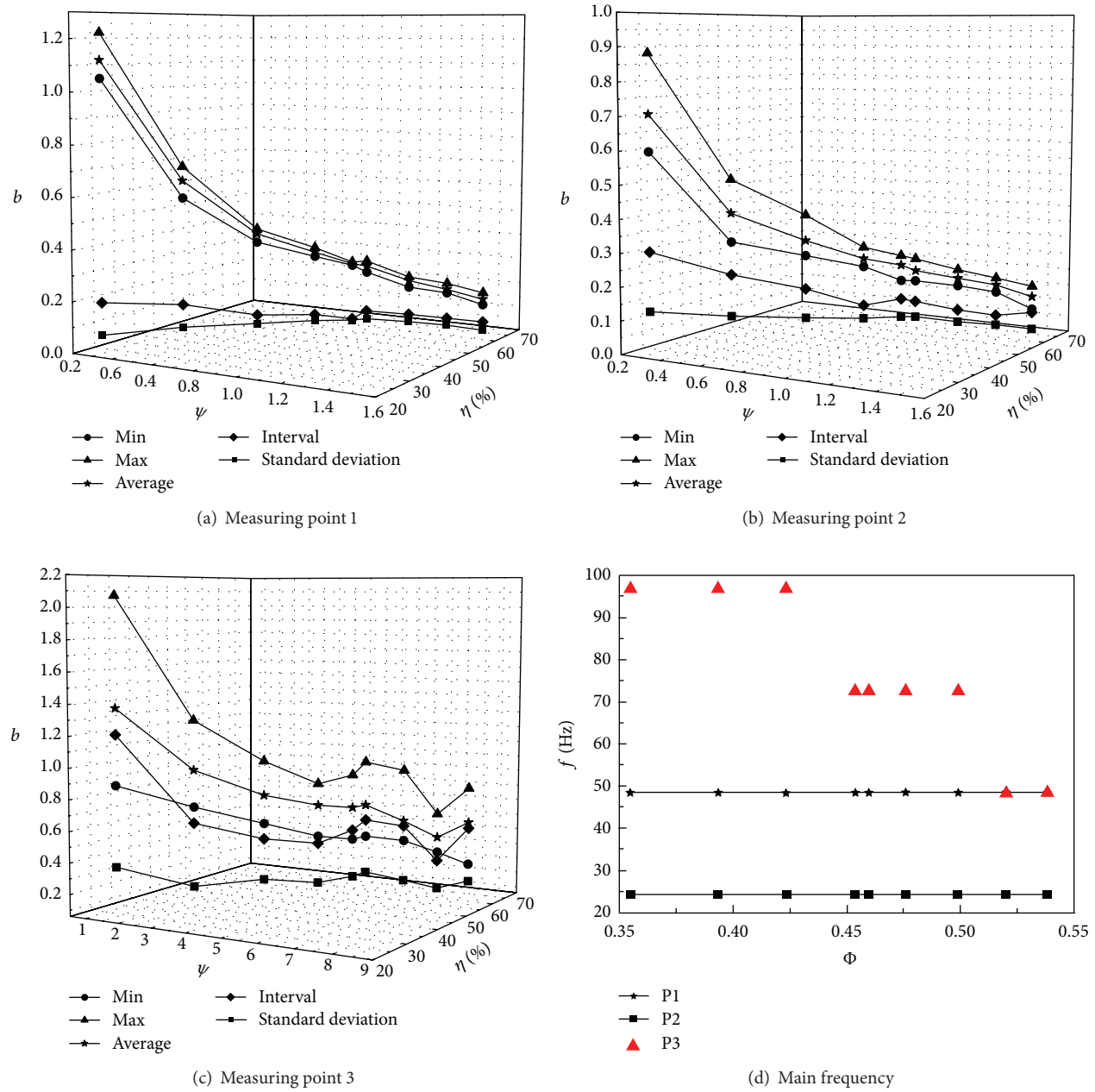


(a) Measuring point 1

(b) Measuring point 2

(c) Measuring point 3

(d) Main frequency

Figure 14: Ratio value $b$ and main frequency of measuring points.

circular rector of the outlet of the guide vane is large, and it is also resulted from the characteristics of the structure of the double-helix volute passage.

## 5. Conclusions

The steady turbulent flow in the mixed-flow pumping system was simulated based on software ANSYS CFX. Both the internal flow fields and the external performance of the system were calculated and predicted. The flow fields of the double-helix volute passage and the hydraulic performance of impeller were analyzed.

Comparing the calculated results with the experimental data, a good agreement was found for head between calculated and measured results. While the deviation of the efficiency between calculated and measured results does exist in non design points which need to be improved.

The flow in the double-helix volute passage is a spiral movement combing axial and rotary flow; static pressure distribution is symmetric. The uniformity of axial velocity distribution and velocity-weighted average swirl angle at the outlet section is relatively low. The hydraulic loss of double-helix volute passage decreases first and then increases with the increase of flow rate.

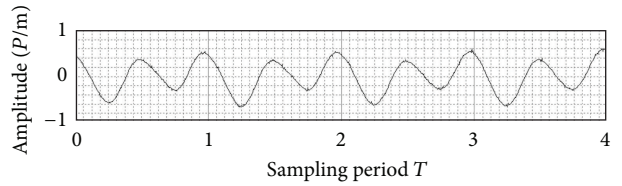


(a) Measuring point 1 $\psi = 1.223$

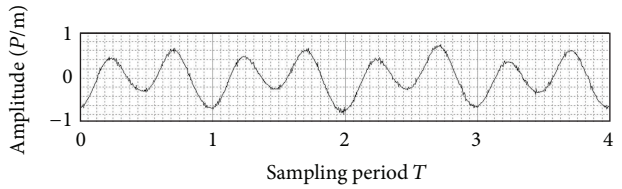


(b) Measuring point 1 $\psi = 0.383$

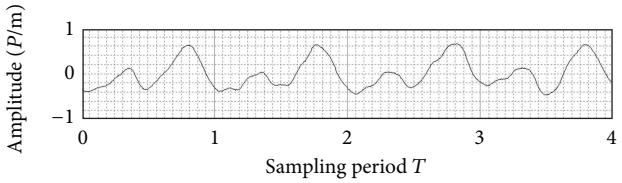


(c) Measuring point 2 $\psi = 1.223$

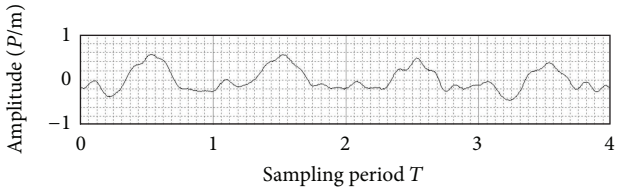


(d) Measuring point 2 $\psi = 0.383$

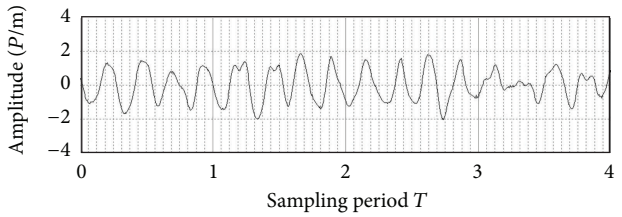


(e) Measuring point 3 $\psi = 1.223$

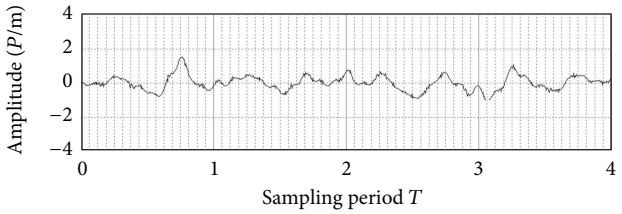


(f) Measuring point 3 $\psi = 0.383$

Figure 15: Time-domain chart of different operating conditions.

Static pressure on the blade surface has a regular distribution with higher static pressure on pressure side and lower one on the suction side. Cavitation region is easily to occur on the leading edge of the suction side. The axial force decreases gradually with the increase of flow rate, while the radial force decreases first and then increases.

Flow rate variation has a little effect on double amplitude peak value of the "$\omega$" back wall of inlet passage and the impeller inlet but has a great effect on that of double-helix volute passage. The time-domain spectrums show that the static pressure, fluctuation curves at the rotor inlet, the "$\omega$" back wall of inlet passage, and the double-helix volute passage are period. The results of experiment and numerical simulation show that the hydraulic performance of the double-helix volute passage has an important influence on the efficiency of pumping system.

## Nomenclature

$p^*$: Converted pressure
$u_j$: Velocity component
$\mu_{\text{eff}}$: Effective viscous coefficient
$\mu$: Fluid dynamic viscosity
$\rho$: Fluid density
$k$: Turbulent kinetic energy
$\omega$: Turbulence frequency
$\Phi$: Flow rate coefficient
$\psi$: Head coefficient
$\beta$: Blade angle
$\zeta$: Pressure recovery coefficient
$\theta$: Velocity-weighted average swirl angle
$N$: Rotating speed
$Q$: Volume flow rate
$H$: Head
$D$: Diameter of impeller
$g$: Acceleration of gravity
$n_s$: Specific speed
$V_{z+}$: Uniformity of axial velocity distribution
$\Delta h$: Hydraulic loss.

## Acknowledgments

This project is supported by National Natural Science Foundation of China (Grant no. 51279173) and Natural Science Major Program of JiangSu Provincial Colleges (Grant no. 11KJA570001). Support for construction/assembly of the facility was also provided by Hydrodynamic Engineering Laboratory of Jiangsu Province.

## References

[1] W. C. Zierke, W. A. Straka, and P. D. Taylor, "Experimental investigation of the flow through an axial-flow pump," *Journal of Fluids Engineering*, vol. 117, no. 3, pp. 485–490, 1995.

[2] F.-J. Wang, Y.-J. Li, G.-H. Cong, W.-E. Wang, and H.-S. Wang, "CFD simulation of 3D flow in large-bore axial-flow pump with half-elbow suction sump," *Journal of Hydrodynamics B*, vol. 18, no. 2, pp. 243–247, 2006.

[3] D. Kaya, "Experimental study on regaining the tangential velocity energy of axial flow pump," *Energy Conversion and Management*, vol. 44, no. 11, pp. 1817–1829, 2003.

[4] H. Gao, W. Lin, and Z. Du, "Numerical flow and performance analysis of a water-jet axial flow pump," *Ocean Engineering*, vol. 35, no. 16, pp. 1604–1614, 2008.

[5] Y.-J. Li and F.-J. Wang, "Numerical investigation of performance of an axial-flow pump with inducer," *Journal of Hydrodynamics B*, vol. 19, no. 6, pp. 705–711, 2007.

[6] D.-S. Zhang, W.-D. Shi, B. Chen, and X.-F. Guan, "Unsteady flow analysis and experimental investigation of axial-flow pump," *Journal of Hydrodynamics B*, vol. 22, no. 1, pp. 35–43, 2010.

[7] D. Wu, L. Wang, and Z. Bao, "Numerical simulation of flow in open-type mixed flow pump and options of the discharge structures," *Chinese Journal of Mechanical Engineering*, vol. 44, no. 8, pp. 90–96, 2008.

[8] K. Lin, S. L. Cao, B. S. Zhu, and L. Lu, "Flow computations for the design of high specific speed mixed-flow pumps," *Journal of Tsinghua University*, vol. 44, no. 8, pp. 90–96, 2008.

[9] H. Bing, L. Tan, S. L. Cao, and L. Lu, "Prediction method of impeller performance and analysis of loss mechanism for mixed-flow pump," *Science China Technological Sciences*, vol. 55, no. 7, pp. 1988–1998, 2012.

[10] A. M. Felix, H. Peter, and D. Philippe, "CFD calculation of a mixed flow pump characteristic from shutoff to maximum flow," *Journal of Fluids Engineering*, vol. 124, no. 3, pp. 798–802, 2002.

[11] A. Posa, A. Lippolis, R. Verzicco, and E. Balaras, "Large-eddy simulations in mixed-flow pumps using an immersed-boundary method," *Computers and Fluids*, vol. 47, no. 1, pp. 33–43, 2011.

[12] J.-H. Kim, H.-J. Ahn, and K.-Y. Kim, "High-efficiency design of a mixed-flow pump," *Science China Technological Sciences*, vol. 53, no. 1, pp. 24–27, 2010.

[13] H. Zhu, S. Yuan, H. Liu, and W. Shi, "Numerical simulation of the 3-D flow of a volute-type discharge passage in large pumping stations," *Transactions of the Chinese Society of Agricultural Machinery*, vol. 38, no. 10, pp. 49–53, 2007.

[14] Y. Li, H. Yan, Q. Ge, S. Chen, and D. Yan, "Research on efficient pump device with new type volute passage of large pumping station," *Journal of Hydroelectric Engineering*, vol. 28, no. 6, pp. 200–205, 2009.